Research Article

Journal of Environmental Nanotechnology

Microwave-assisted Synthesis of Polypyrrole-functionalized Predominantly 2H-phase $MoSe_2$: Structural, Optical, Thermal, Morphological, and Electrochemical Investigations

Aparna Unnikrishnan and J. Balavijayalakshmi*

Department of Physics, PSGR Krishnammal College for Women, Coimbatore, TN, India

Received: 25.07.20265 Accepted: 24.08.2026 Published: xx.xx.xxxx

*balavijayalakshmiroopa@gmail.com

ABSTRACT

Molybdenum selenide ($MoSe_2$)-conducting polymer composites are garnering interest as electrode materials because of their tunable physicochemical and electrochemical properties. However, developing rapid synthesis routes for well-defined $MoSe_2$/polypyrrole (PPy) composites remains challenging. In this study, predominantly 2H-phase molybdenum selenide (MS) and its PPy-functionalized composite (MSP) were synthesized using a rapid 15 min microwave-assisted method. X-ray diffraction (XRD) confirmed the hexagonal 2H-$MoSe_2$ phase with an average crystallite size of 50.0 nm, while the characteristic $MoSe_2$ peaks and PPy-related features indicated composite formation. Raman spectroscopy identified the vibrational modes of $MoSe_2$ and PPy. Field-emission scanning electron microscopy (FE-SEM) revealed a hierarchical cauliflower-like morphology, with PPy distributed over the $MoSe_2$ nanostructures, while energy-dispersive X-ray spectroscopy (EDX) indicated near-ideal Mo stoichiometry. UV–Vis spectroscopy showed a reduced optical band gap of 1.58 eV for MSP compared with 1.77 eV for MS and 2.01 eV for PPy. Thermogravimetric analysis (TGA) showed improved thermal stability after PPy incorporation. Cyclic voltammetry (CV) in an I_3^-/I^- redox electrolyte showed substantially higher redox peak currents for MSP than MS, demonstrating enhanced charge-transfer activity. These findings highlight PPy functionalization as an effective approach to tailoring $MoSe_2$ for electrochemical applications, particularly in dye-sensitized solar-cell counter electrodes.

Keywords: PPy; 2H-$MoSe_2$; Microwave-assisted synthesis; Nanocomposite; Optical band gap; Cyclic voltammetry.

1. INTRODUCTION

Energy has become a fundamental component of daily life, serving as both a primary driving force and an indicator of quality of life. The increase in carbon emissions and the threat of global warming necessitate a transition towards renewable energy sources. Researchers have developed and evaluated technologies such as solar and wind power to support sustainable, cost-effective energy systems. Continued reliance on finite fossil-fuel reserves cannot meet escalating energy demands, highlighting the critical importance of alternative energy sources and advanced functional materials for energy conversion and storage. Among these materials, layered transition-metal dichalcogenides and conducting-polymer hybrids have attracted particular interest owing to their tunable electronic structure, high surface area, and versatile electrochemical behavior.

Transition metal dichalcogenides (TMDCs) are an expanding field of study because of their distinct chemical and physical characteristics. They have large active surfaces with many sites available for catalytic use. TMDCs are composed of transition metals and chalcogen atoms (S, Se, and Te), forming layers held together by weak van der Waals forces. They are attractive for solar energy applications owing to their high surface-to-volume ratio, low cost, and environmental benefits (Sheela *et al.* 2023; Manimekalai *et al.* 2025). Within the broad TMDC family, their tunable electronic structure and layered morphology have enabled significant progress in electrocatalysis, supercapacitors, and photovoltaic interfaces, positioning TMDCs as versatile building blocks for next-generation energy devices. Molybdenum diselenide ($MoSe_2$) is a TMDC that shows promise for energy applications. It is a two-dimensional material in which selenium is the chalcogen and molybdenum is the metal (Balasingam *et al.* 2015; Sowbakkiyavathi *et al.* 2020). $MoSe_2$ is stable, affordable, and catalytically active. Its unique structure, with three atomic layers held by weak forces, makes it easy to separate and provides a high surface area and better electronic conductivity (Kashyap *et al.* 2025).

Polypyrrole (PPy), a widely studied conducting polymer, has attracted significant attention owing to its exceptional electrical and electrochemical properties. As a π-conjugated organic polymer, PPy exhibits high

electrical conductivity, excellent environmental stability, and facile synthesis, making it a promising material for diverse electronic and energy applications. Its low cost, simple fabrication, and flexibility make it an attractive electrode material, although limited mechanical robustness and moderate intrinsic catalytic activity can constrain performance when used alone. Incorporating TMDCs into a PPy matrix couples the dichalcogenide's catalytic sites and layered charge-transport pathways with the conductive polymer network. In particular, integrating PPy with $MoSe_2$ helps overcome the individual limitations of each material, leading to better structural stability, higher overall conductivity, and faster interfacial charge transfer, with $MoSe_2$ supplying catalytic sites and layered pathways for electron transport while PPy strengthens the structure and promotes charge transfer.

Despite these advantages, reports that combine $MoSe_2$ with PPy remain limited and have largely relied on relatively slow or multi-step routes. For instance, $MoSe_2$/PPy composites have been prepared by *in situ* hydrothermal synthesis for photocatalytic dye degradation (Mittal and Khanuja, 2021), and cobalt-doped 2D-$MoSe_2$/PPy carbon nanofibers have been fabricated by electrospinning for electrochemical sensing (Celik *et al.* 2024). Analogous $MoSe_2$/polyaniline systems synthesized by *in situ* oxidative polymerization or as composite nanofibers have similarly been directed toward photocatalysis and dye-sensitized solar-cell counter electrodes (Mittal and Khanuja, 2019; Sowbakkiyavathi *et al.* 2020; Singh *et al.* 2021). Microwave-assisted synthesis has recently emerged as an efficient route for preparing transition-metal dichalcogenide nanostructures because it provides rapid and uniform heating, shorter reaction times, and improved control over particle nucleation and growth. Compared with conventional hydrothermal methods, microwave irradiation enables faster formation of $MoSe_2$ nanostructures with enhanced crystallinity and surface activity. However, integrating microwave-synthesized $MoSe_2$ with conductive polymers such as PPy, and fully understanding the resulting composite's physicochemical properties, remains relatively unexplored.

In this study, predominantly 2H-phase molybdenum diselenide (2H-$MoSe_2$) and its PPy-functionalized composite ($MoSe_2$/PPy) were synthesized via a rapid microwave-assisted method, which offers several advantages over conventional techniques, including rapid reaction rates, uniform volumetric heating, energy efficiency, and improved control over crystallinity and morphology. PPy was prepared separately by ultrasonic-assisted oxidative chemical polymerization and incorporated into the $MoSe_2$ matrix. The structural, optical, thermal, morphological, and electrochemical properties of pristine $MoSe_2$, PPy, and the $MoSe_2$/PPy composite were systematically investigated using X-ray diffraction, Fourier-transform infrared and Raman spectroscopy, field-emission scanning electron microscopy coupled with energy-dispersive X-ray analysis, UV–Vis spectroscopy, thermogravimetric analysis, and cyclic voltammetry to establish how PPy functionalization modifies the physicochemical behavior of 2H-$MoSe_2$.

2. MATERIALS AND METHODS

2.1 Materials

Sodium molybdate (Na_2MoO_4, 99.99%), selenium (Se, 99.99%), and hydrazine hydrate ($N_2H_4.H_2O$, 98%) were used to synthesize $MoSe_2$. Hydrochloric acid ($HCl.H_2O$, 99.96%), ferric chloride ($FeCl_3$, 96%), and a pyrrole monomer (C_4H_4NH, 99%) were used to synthesize PPy.

2.2 Synthesis of $MoSe_2$ Nanoparticles

The microwave-assisted synthesis of $MoSe_2$ was carried out by dispersing 0.632 g (8 mmol) of selenium powder in 20 mL of hydrazine hydrate ($N_2H_4 \cdot H_2O$) under magnetic stirring for 10 min. Subsequently, 0.824 g (3.4 mmol) of $Na_2MoO_4 \cdot 2H_2O$ solution was added dropwise to the selenium–hydrazine suspension under continuous stirring to obtain a homogeneous reaction mixture. The resulting solution was subjected to microwave irradiation at 360 W and 160 °C for 15 min. After completion of the reaction, the precipitate was collected by centrifugation at 6000 rpm for 10 min, washed thoroughly with ethanol, and dried in a vacuum oven at 60 °C for 24 h before further characterization.

The microwave synthesis parameters (360 W, 160 °C, and 15 min) were optimized through a series of preliminary experiments. These conditions provided rapid nucleation and uniform crystal growth of $MoSe_2$ while minimizing reaction time and energy consumption. Microwave irradiation provides homogeneous volumetric heating, enabling efficient precursor reduction and promoting the formation of well-crystallized $MoSe_2$ nanoparticles. Hydrazine hydrate served both as the solvent and reducing agent, while the Na_2MoO_4-to-Se precursor ratio was maintained close to the stoichiometric Mo ratio of 1:2 to facilitate the formation of phase-pure 2H-$MoSe_2$.

For composite preparation, the PPy loading was fixed at 100 mg based on preliminary optimization studies. Lower PPy contents resulted in incomplete surface coverage of $MoSe_2$, whereas higher loadings partially masked the characteristic diffraction features of $MoSe_2$ and could adversely affect its intrinsic structural characteristics. The selected loading therefore ensured uniform polymer coating while preserving the crystallinity of the $MoSe_2$ phase.

To evaluate the reproducibility of the synthesis, the microwave-assisted preparation was repeated three times under identical experimental conditions.

The preparation method for $MoSe_2$ is schematically illustrated in Fig 1.

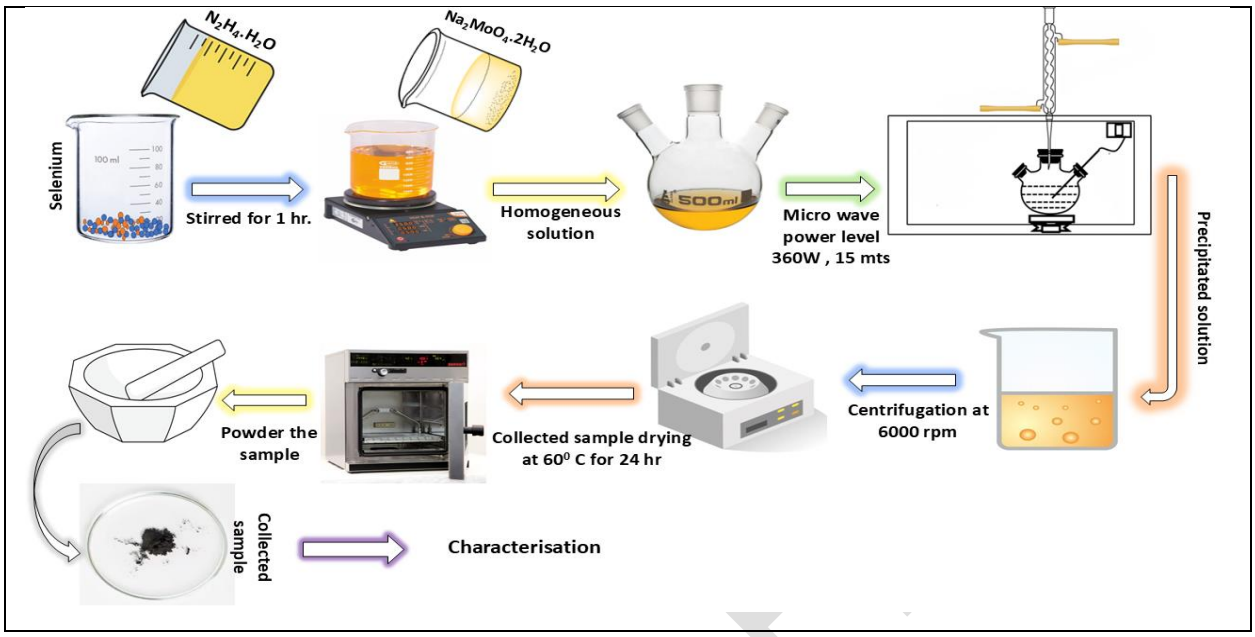

Fig. 1: Schematic illustration of the microwave-assisted synthesis of $MoSe_2$

2.3 Synthesis of $MoSe_2$/PPy Hybrids

PPy was synthesized by oxidative chemical polymerization (OCP), and the schematic procedure is shown in Fig. 2. In a standard OCP procedure, 7.1 g of $FeCl_3$ powder was mixed with 1 M HCl while being stirred in an ice bath at temperatures between 0–5 °C for 30 min to create an oxidant solution. Subsequently, 6.1 mL of pyrrole monomer was added to the solution and refluxed for 16 h at room temperature. The resulting product was filtered and washed repeatedly with methanol and acetone. The final black product was dried overnight in an oven set at 60 °C. The $MoSe_2$/PPy sample was prepared following the same method used for synthesizing $MoSe_2$ nanoparticles, with the addition of 100 mg of ultrasonically dispersed PPy to the Mo salt solution (Mittal and Khanuja, 2021; Celik *et al.* 2024). The synthesized samples $MoSe_2$, PPy, and the composite $MoSe_2$/PPy are referred to as MS, PPy, and MSP, respectively.

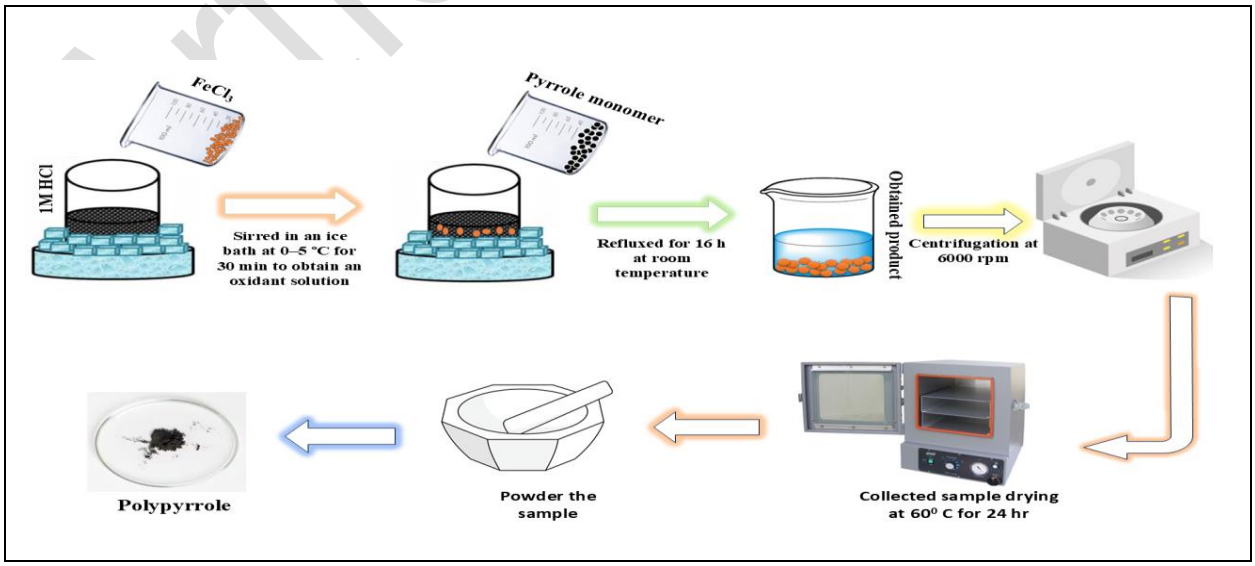

Fig. 2: PPy synthesis *via* oxidative chemical polymerization

3. CHARACTERIZATION TECHNIQUES

XRD was used to confirm the effective synthesis and purity of the materials using a Bruker D8 instrument with a Cu X-ray source, scanning from 5° to 60° at a rate of 2°/min. FTIR, conducted using Bruker Alpha II, identified functional groups in the spectral range of 400–4000 cm^{-1}. FE-SEM (Carl Zeiss Model Supra 55) was used to evaluate the surface morphology and particle size after gold coating for 90 s, at an accelerating voltage of 15 kV under high-vacuum conditions. Raman spectra were recorded at room temperature using a Nano Tech1 (QEB0120) instrument. TGA, performed on an SII 6300 EXSTAR instrument, assessed thermal stability under a nitrogen flow of 200 mL/min from 25 °C to 600 °C at a heating rate of 10 °C/min. Cyclic voltammetry was performed using a Biologic SP-240 electrochemical workstation to study electrocatalytic activity, redox potential, and cyclic stability. UV–Vis absorption spectroscopy using a Shimadzu UV-2600i (200–1100 nm) was employed to determine the optical bandgap *via* Tauc plot analysis.

4. RESULTS AND DISCUSSION

4. 1 Characterization of the Synthesized Materials

4.1.1 Functional Group Characteristics

The FTIR spectra of the synthesized MS, PPy, and MSP samples, recorded in the range of 400–4000 cm^{-1}, are presented in Fig. 3 and are used to identify the characteristic functional groups. For MS, the band near 636 cm^{-1} is attributed to a surface Mo–O-related vibration arising from slight surface oxidation of the $MoSe_2$, since the fundamental Mo–Se stretching modes appear in the far-infrared region (below ~350 cm^{-1}) and are more reliably resolved by Raman spectroscopy. The band at 893 cm-¹ corresponds to the Se–Mo–Se bending mode. This mode is characteristic of the trigonal prismatic coordination geometry of $MoSe_2$, highlighting its layered crystalline structure and the weak van der Waals forces between layers that allow for out-of-plane vibrations (Mittal and Khanuja, 2019).

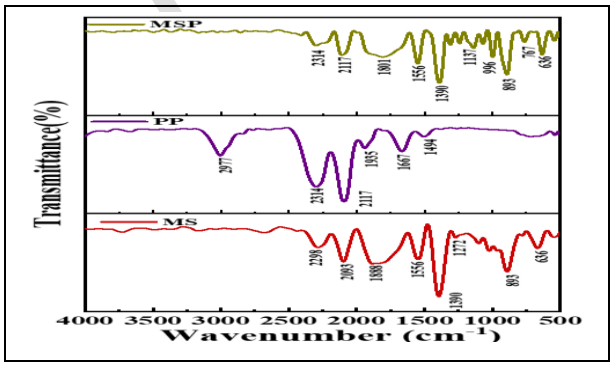

Fig. 3: FTIR spectra of MS, PPy, and MSP

Moving to higher wavenumbers, the band at 1272 cm^{-1} can be associated with C–O stretching vibrations, potentially from adsorbed organic molecules or decomposition products from precursors. These organic residues may adhere to the defect sites or the edges of the $MoSe_2$ lattice through weak chemisorption or physisorption. At 1390 cm^{-1}, the symmetric stretching vibrations of carbonate ions (CO_3^{2-}) are observed. These ions are likely adsorbed onto the surface owing to exposure to atmospheric CO_2, with their resonance-stabilized C–O bonds splitting into symmetric and asymmetric modes (Siddiqui *et al.* 2018).

The band at 1556 cm^{-1} is indicative of vibrational modes associated with surface-adsorbed water or hydroxyl groups. These vibrations likely arise from the H–O–H bending mode in water molecules hydrogen-bonded to the $MoSe_2$ surface, stabilized by van der Waals forces or weak hydrogen bonding. Additionally, this peak suggests possible interactions between selenium and adsorbed oxygen-containing species, suggesting surface oxidation. The weak feature near 1888 cm^{-1} is assigned to an overtone/combination band rather than a fundamental metal–oxygen stretch, as fundamental Mo–O stretching vibrations occur at much lower wavenumbers (~800–1000 cm^{-1}). (Mittal and Khanuja, 2021).

The weak band near 2093 cm^{-1} falls in the region characteristic of atmospheric or physisorbed species (e.g., dissolved CO/CO_2 and combination modes) rather than a metal–selenide vibration, since Mo–Se fundamental vibrations occur in the far-infrared region. The structural integrity of the $MoSe_2$ lattice is instead confirmed by XRD and Raman analyses (Mittal and Khanuja, 2021).

For PPy, the band at 1494 cm^{-1} corresponds to C=C stretching vibrations within the pyrrole ring. This vibration indicates the aromatic structure of PPy, and the delocalized π-electron system in the pyrrole ring produces a characteristic stretching mode in this region, confirming the aromatic nature of the PPy chain. The band at 1667 cm^{-1} can be attributed to C=O stretching vibrations. This suggests the presence of carbonyl groups, likely introduced during polymer synthesis or resulting from partial oxidation. The C=O bond is polar because of the large electronegativity difference between carbon and oxygen, leading to strong absorption in this region. Carbonyl groups may arise from dopants or from atmospheric oxygen. The broad band near 2977 cm^{-1} corresponds to C–H stretching vibrations associated with the pyrrole units. This absorption confirmed intact pyrrole units in the polymer backbone (Kashyap *et al.* 2025). For sample MSP, the weak features near 2314 cm^{-1} and 2117 cm^{-1}, common to both PPy and the composite, lie in a region associated with atmospheric CO_2 and combination/overtone modes and are not diagnostic of specific functional groups. More

significantly, the principal bands of the composite closely match those of $MoSe_2$ while retaining the characteristic C=C pyrrole-ring band of PPy near 1494 cm^{-1}, indicating successful incorporation of PPy alongside the dominant $MoSe_2$ structural features.

4.1.2 Structural Analysis

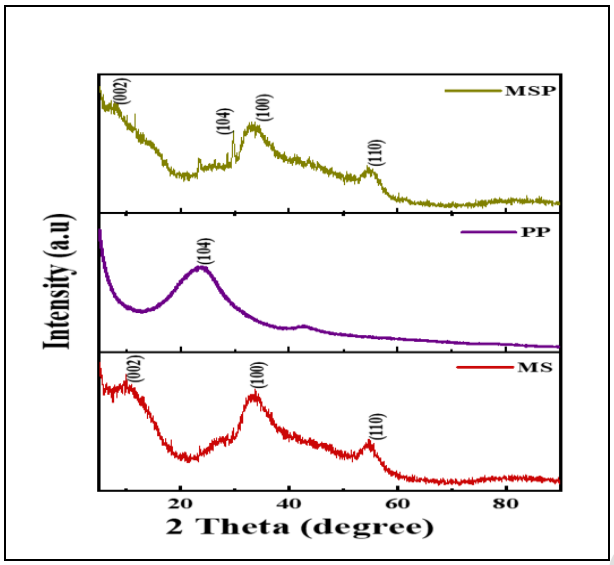

Fig. 4: XRD patterns of MS, PPy, and MSP

XRD analysis, performed over a scanning range of 5°–60° at 2°/min, is used to confirm the successful synthesis and purity of the materials, and the resulting diffraction patterns of MS, PPy, and MSP are shown in Fig. 4. The XRD spectrum of the $MoSe_2$ synthesized *via* the microwave-assisted method shows diffraction peaks at 12.8°, 33.6°, and 54.5°, corresponding to the (002), (100), and (110) planes, respectively. These peaks matched JCPDS No. 87-2419, confirming the material's structural integrity and phase purity. The d-spacings (Å) of each peak with respect to the corresponding hkl plane were 6.91, 2.80, and 1.63, respectively, confirming the successful synthesis of hexagonal 2H-$MoSe_2$ (Vattikuti *et al.* 2020). The average crystallite size of $MoSe_2$ was calculated using the Debye–Scherrer equation (Eq. 1) and was found to be 50.0 nm. (Table 1).

$$D = \frac{K\lambda}{\beta \cos\theta} \quad \ldots (1)$$

The lattice constants were calculated using Equation (2) for the hexagonal system (a = b ≠ c) and were found to be a = 3.28 Å and c = 12.93 Å. These values are consistent with reported values, indicating no significant lattice distortion or detectable impurity phases.

$$1/d^2 = (h^2+k^2)/ a^2 + l^2/c^2 \quad \ldots (2)$$

For the PPy sample, the dominant broad peak observed at approximately 24° is a well-established feature of PPy and corresponds to the π-π stacking of the conjugated polymer chains. This peak reflects the periodic arrangement of the aromatic pyrrole rings, which align in a planar manner owing to the delocalized π-electron system. According to the Debye–Scherrer equation, the average crystallite size of PPy was found to be 9.04 nm. The semi-crystalline nature of PPy results in a broadened peak rather than a sharp one, signifying that the material has a limited long-range order, which is typical of conducting polymers. The weak, broad peak at approximately 42° likely arises from secondary scattering, possibly due to less-ordered phases or interplanar spacing influenced by PPy's inherent chain flexibility. This peak is not indicative of impurities, as impurities typically produce sharper, well-defined peaks owing to their crystalline nature. Instead, it reflects the subtle structural features of the polymer, possibly related to hydrogen bonding between chains or weakly ordered domains (Zhang *et al.* 2015).

Table 1. Comparison of crystallite sizes of MS and MSP samples at different XRD peaks

Material	Peak No.	2θ (°)	θ (°)	FWHM (°)	FWHM, β (rad)	D (nm)	Average D (nm)
MS	1	12.8	6.4	0.1591	0.002776	50.2	50.01
	2	33.6	16.8	0.0888	0.00155	93.5	
	3	54.5	27.25	1.4132	0.024665	6.34	
MSP	1	9.8	4.9	0.1088	0.0019	73.2	43.16
	2	33.0	15.0	0.1901	0.003318	43.6	
	3	55.2	27.6	0.7087	0.012369	12.7	

The XRD spectrum of the MSP composite confirmed the successful incorporation of PPy into pure $MoSe_2$. The characteristic PPy peak at 24° was clearly present. Introducing PPy shifted the $MoSe_2$ characteristic peak at 12.8° (002) to a slightly lower angle and reduced its intensity (Dai *et al.* 2022). This may result from partial disruption of the $MoSe_2$ layered structure due to interactions with the PPy chains, likely through π-π stacking or weak van der Waals forces. In contrast, the $MoSe_2$ peaks at 33.6° and 54.5 ° show a slight increase in

intensity. This change may result from PPy influencing the reorganization or alignment of $MoSe_2$ crystallites during composite synthesis. The preserved PPy peak at 24° and the changes in $MoSe_2$ peak intensities demonstrate the successful integration of PPy within the $MoSe_2$ structure, modifying its local environment and crystallinity while maintaining the structural integrity of both components. The average crystallite size of the prepared $MoSe_2$/PPy nanocomposite was found to be 43.16 nm. For comparison, the 50.0 nm average crystallite size and lattice parameters (a = 3.28 Å and c = 12.93 Å) obtained here are consistent with those reported for hexagonal 2H-$MoSe_2$ prepared by slower *in situ* selenization and hydrothermal routes (Upadhyay and Pandey, 2021; Wang *et al.* 2023), confirming that the 15-min microwave route affords comparable crystallinity in a fraction of the reaction time (typically several hours) required by those methods (Vattikuti *et al.* 2020).

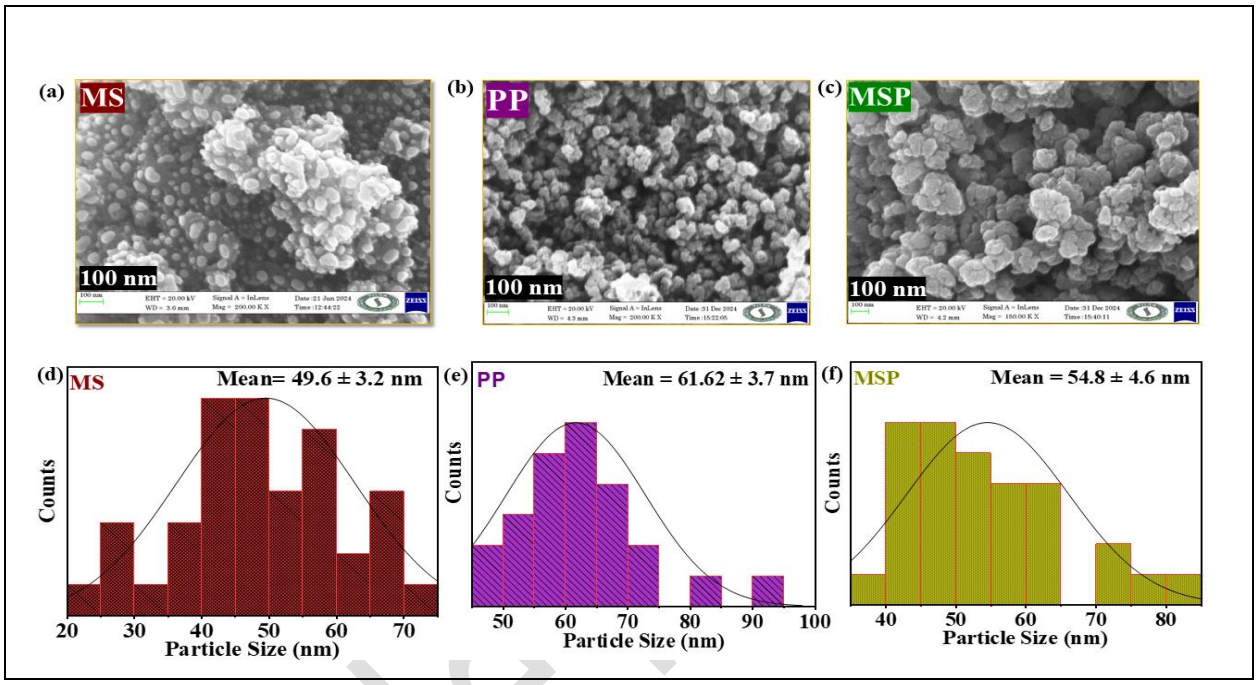

Fig. 5: FE-SEM images of (a) MS, (b) PPy, and (c) MSP, and particle size distributions of (d) MS, (e) PPy, and (f) MSP

4.1.3 Morphological Analysis

FE-SEM was employed to examine the surface morphology and the particle size distribution histograms of MS, PPy, and MSP (Fig. 5). The FE-SEM image of MS synthesized *via* the microwave-assisted method exhibits a bead-like or nano-pebble morphology composed of densely packed spherical nanostructures distributed across the surface (Upadhyay and Pandey, 2021). Both individual nanoparticles and small agglomerated clusters can be observed, indicating the formation of nanosized $MoSe_2$ particles with relatively uniform dispersion (Zhang *et al.* 2020). Particle size distribution analysis from the FE-SEM image (Fig. 5d), based on measurements of 100 particles, reveals an average particle size of 49.6 ± 3.2 nm.

The FE-SEM image of PPy displays a densely agglomerated granular morphology forming an interconnected porous network (Mittal and Khanuja, 2019). The polymer particles appear as clustered nanogranules with a rough surface texture, typical of PPy synthesized *via* oxidative polymerization (Wang *et al.* 2023). The particle size distribution histogram (Fig. 5e), based on measurements of 100 particles, indicates an average particle size of 61.62 ± 3.7 nm.

The FE-SEM image of the MSP composite exhibits a hierarchical cauliflower-like morphology, where $MoSe_2$ nanostructures are uniformly decorated with PPy particles. Compared with pristine MS, the MSP composite shows a more interconnected and rough surface structure, indicating effective incorporation of PPy onto the $MoSe_2$ framework (Mittal and Khanuja, 2021). These morphological features are advantageous for electrochemical applications because increased surface roughness and porosity provide a larger active surface area for electrolyte interaction. The particle size distribution analysis (Fig. 5f), based on the measurement of 100 particles, shows an average particle size of 54.8 ± 4.6 nm for the MSP composite.

4.1.4 Elemental Analysis

Figs. 6(a–c) show the EDX spectra of MS, PPy, and MSP. EDX analysis of the MS sample provided insight into its elemental composition and confirmed its successful synthesis.

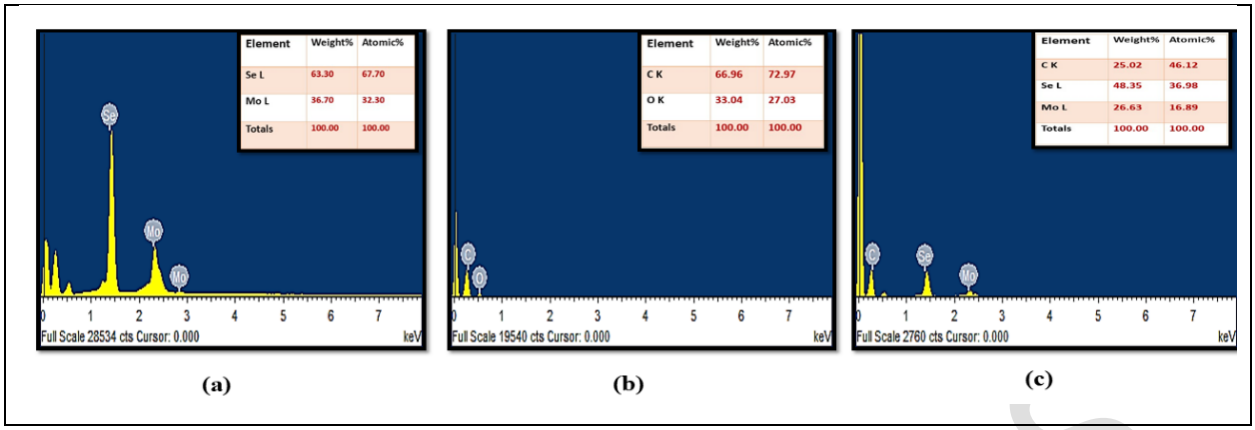

Fig. 6: EDX spectra of (a) MS, (b) PPy, and (c) MSP.

The data reveal that Se is present at 63.30% by weight and 67.70% by atomic percentage, whereas Mo accounts for 36.70% by weight and 32.30% by atomic percentage. This ratio was close to the ideal 1:2 stoichiometry expected for $MoSe_2$, indicating that the synthesis process effectively incorporated selenium in the right proportion with Mo (Mittal and Khanuja, 2019).

The higher atomic percentage of selenium than molybdenum aligns with the structural characteristics of TMDCs, in which each molybdenum atom bonds to two selenium atoms in a layered arrangement. Furthermore, the absence of other elements in the EDX spectrum suggests that the sample has high purity. PPy is a conducting polymer primarily composed of carbon, hydrogen, and nitrogen. However, this analysis detected only carbon and oxygen. The significant oxygen signal suggests possible oxidation, which can occur due to environmental exposure and synthesis conditions. The high carbon content confirmed the organic nature of the polymer, supporting its characteristic conjugated backbone structure, which is responsible for its electrical conductivity. The absence of nitrogen in the EDX spectrum might be due to limitations in detecting light elements, such as nitrogen, in standard EDX systems, as nitrogen peaks can be weak. (Zhang *et al.* 2015).

The EDX analysis confirmed successful functionalization. The presence of carbon, selenium, and molybdenum in distinct proportions highlights the structural modifications introduced by PPy coating. With carbon accounting for 25.02% by weight and 46.12% by atomic percentage, it is evident that the PPy component was well incorporated into the material (Vishnu and Badhulika, 2019). The high atomic percentage of carbon suggests a significant presence of the polymer, likely forming a surface layer or intercalating within the $MoSe_2$ structure of selenium and molybdenum, with weight percentages of 48.35% and 26.63%, respectively, indicating that the $MoSe_2$ structure remained largely intact despite the introduction of PPy (Ma *et al.* 2016). The Mo:Se ratio remains close to the expected stoichiometry of $MoSe_2$, confirming that functionalization does not disrupt the material's fundamental layered arrangement (Dhanasekaran *et al.* 2024).

4.1.5 Vibrational Analysis by Raman Spectroscopy

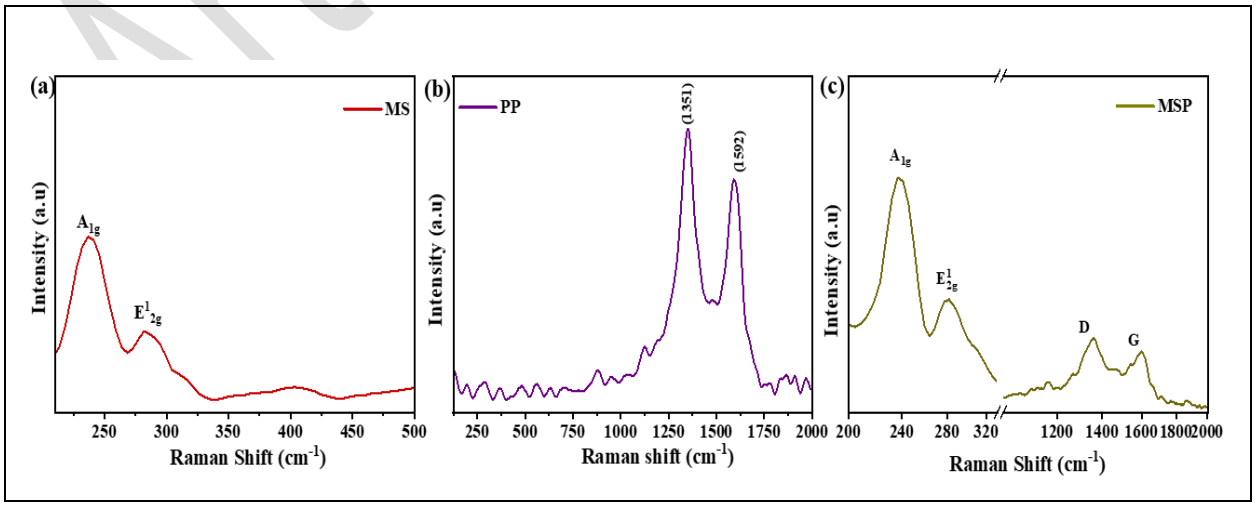

Fig. 7: Raman spectra of (a) MS, (b) PPy, and (c) MSP

Raman spectra were recorded at room temperature, and the corresponding spectra of (a) MS, (b) PPy, and (c) MSP are illustrated in Fig. 7. In the Raman spectra of MS, two distinct peaks were observed at 242 cm^{-1} and 285 cm^{-1}, which correspond to the A_1g and E^1_2g bands, respectively. The emergence of peaks at 240 cm^{-1} and 295 cm^{-1} indicates the presence of $MoSe_2$. The shift of the first characteristic peak from 242 to 240 cm^{-1} may be attributed to a change in the bulk behavior of the nanoparticles towards a monolayer. The enhancement of the A_1g mode and the reduction of the E^1_2g mode resulted from various chemical forces between the layers.

In Fig. 7 (b), the peak at 1351 cm^{-1} is attributed to the D-band (disordered band), which corresponds to the ring stretching vibrations involving nitrogen atoms in the PPy backbone. This band is often associated with the presence of structural defects, amorphous character, or interactions between polymer chains. The intensity and position of this peak can vary depending on the degree of oxidation and polymerization conditions (Xu *et al.* 2018). The second major peak at 1592 cm^{-1} corresponds to the G-band, which arises from the C=C stretching vibrations within the conjugated polymer backbone. This peak is a key indicator of electronic delocalization and structural integrity of the polymer. A shift or broadening in this peak can indicate variations in doping level, degree of polymerization, or interactions with other materials (Mao *et al.* 2017). In the Raman spectrum of the MSP nanocomposite, a blue shift in the G band and a red shift in the D band were observed due to the addition of $MoSe_2$. The peak intensity of the MSP nanocomposite is higher than that of pristine $MoSe_2$ and PPy, which implies fewer defects in the MSP nanocomposite (Ansari *et al.* 2025). The A_1g (~242 cm^{-1}) and E^1_2g (~285 cm^{-1}) positions agree closely with values reported for 2H-$MoSe_2$ (Balasingam *et al.* 2015; Upadhyay and Pandey, 2021), and the D and G bands match those reported for oxidatively polymerized polypyrrole (Celik *et al.* 2024), corroborating successful hybridization in the composite.

4.1.6 Absorption Spectra and Band Gap

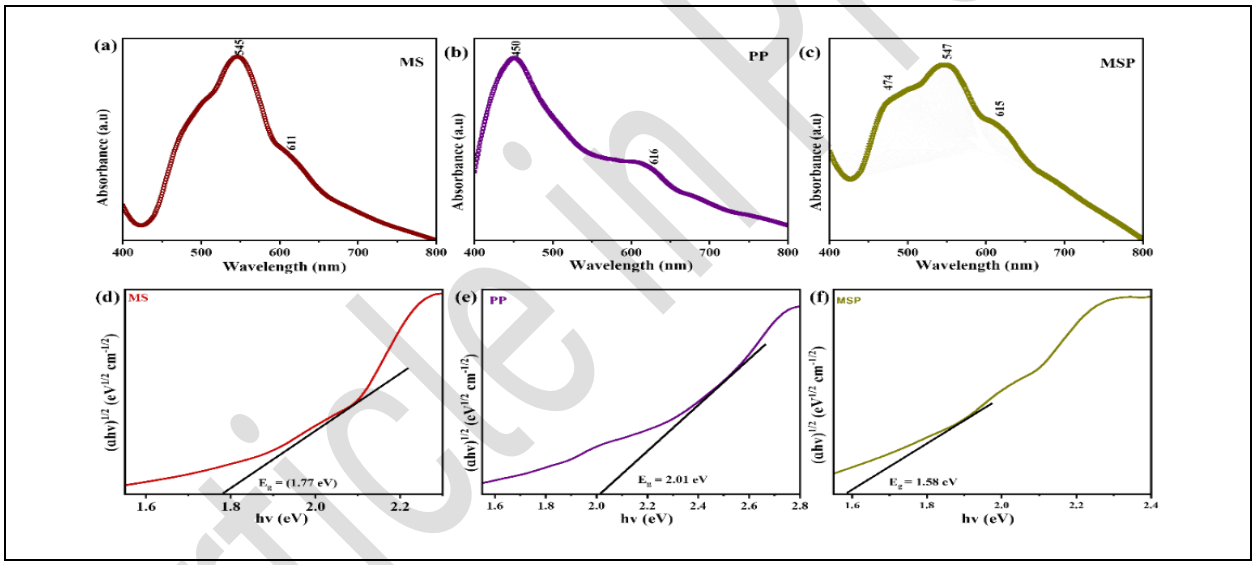

Fig. 8: Absorption spectra of (a) MS, (b) PPy, and (c) MSP, and corresponding Tauc plots of (d) MS, (e) PPy, and (f) MSP

Figs. 8 (a–c) and 8 (d–f) show the absorption spectra and the corresponding band gaps (E_g) of the MS, PPy, and MSP samples, respectively. The optical band gap was determined using the Tauc equation, $(\alpha h\nu)(1/n) = A(h\nu - E_g)$, where α is the absorption coefficient, hν is the photon energy, A is a constant, and E_g is the optical band gap. An indirect allowed transition (n = 2) was assumed, consistent with the indirect gap of 2H-$MoSe_2$, and (αhν)^½ was therefore plotted against hν. The band gap was obtained by linearly extrapolating the linear region of each plot to the energy axis. MS exhibits two distinct peaks, one at approximately 545 nm and the other at 611 nm, which are characteristic of optical transitions. The 545 nm peak corresponds to the A excitonic transition, whereas the broader absorption around 611 nm is attributed to the B excitonic transition (Ansari *et al.* 2025). The Tauc plot derived from the UV-Vis absorption data was used to determine the optical band gap of MS, as shown in Fig. 8 (d). This gives an estimated optical band gap of 1.77 eV. This bandgap value is within the expected range for $MoSe_2$. The slight variation in the band gap value from that of bulk $MoSe_2$ can be attributed to factors such as quantum confinement effects, strain, or defects introduced during synthesis (Kashyap *et al.* 2025). Considering the predominantly multilayer 2H-$MoSe_2$ structure, an indirect allowed transition was assumed for the Tauc analysis. Accordingly, the optical band gaps were estimated from plots of $(\alpha h\nu)^{1/2}$ vs. hν.

$(\alpha h\nu)^{½}$ plots: The approximately linear region of each Tauc plot was selected for linear fitting, and the

fitted line was extrapolated to the photon-energy axis to determine the optical band gap.

Fig. 8(b) shows the absorption spectrum of PP, which exhibits two primary absorption peaks: one centered at approximately 450 nm and the other at 616 nm. The peak at 450 nm corresponds to the π-π* transition of the conjugated polymer backbone, indicating the presence of delocalized electrons in the PPy system. The broad absorption band at a higher wavelength, around 616 nm, indicates the presence of polaronic and bipolaronic states, which contribute to the conductivity of PPy (Vattikuti *et al.* 2020). The Tauc plot derived from the absorption data provides an estimated optical band gap (E_g) of 2.01 eV (Celik *et al.* 2024), as shown in Fig. 8(e).

The UV–Vis absorption spectrum of the MSP sample in Fig. 8 (c) exhibits distinct absorption peaks at approximately 474, 547, and 615 nm. Compared with pristine $MoSe_2$ and PPy, these absorption features suggest enhanced light absorption across a broader wavelength range, potentially due to strong interaction between the conjugated polymer and the transition metal dichalcogenide. The presence of PPy likely induces charge-transfer interactions, which can slightly shift the absorption peaks due to changes in the electronic structure (Chang *et al.* 2010). The PPy-functionalized $MoSe_2$ composite exhibited an estimated optical band gap of 1.58 eV, as illustrated in Fig. 8(f). This value is lower than the band gaps of pristine PPy (~2.01 eV) and $MoSe_2$ (~1.77 eV), indicating a synergistic effect in which the combination of the two materials leads to a reduction in the band gap. This bandgap reduction can be attributed to hybridization of electronic states at the PPy–$MoSe_2$ interface, facilitating improved charge separation and transport properties (Siroha *et al.* 2024). The composite band gap of 1.58 eV is lower than that of pristine $MoSe_2$ (1.77 eV here) and lies below the ~1.7–2.0 eV range commonly reported for $MoSe_2$ and $MoSe_2$/polymer systems, consistent with the band-gap narrowing observed when $MoSe_2$ is coupled with conducting polymers such as PANI and PPy (Sowbakkiyavathi *et al.* 2020; Mittal and Khanuja, 2021).

4.1.7 Thermal Stability and Decomposition Analysis

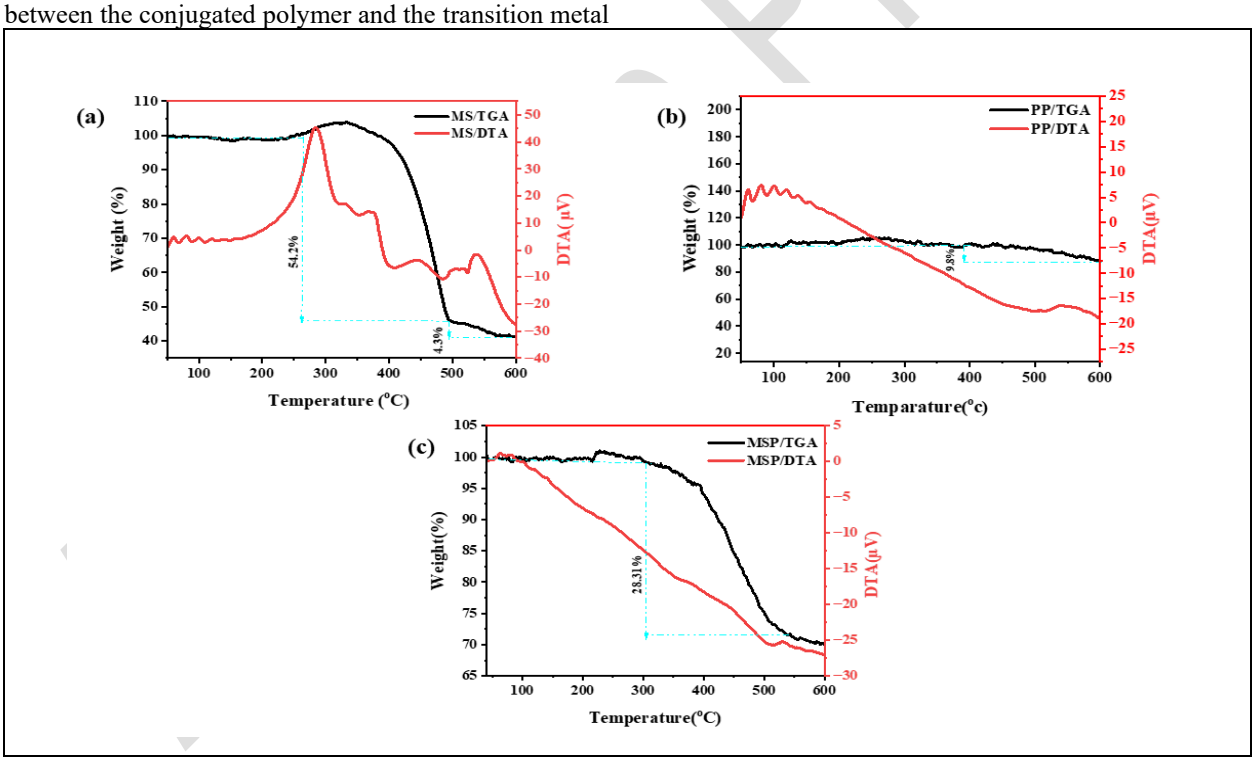

Fig. 9: Thermogravimetric analysis (TGA) and differential thermal analysis (DTA) curves of (a) MS, (b) PPy, and (c) MSP

TGA/DTA curves of (a) MS, (b) PPy, and (c) MSP are shown in Fig. 9. The TGA and DTA of MS (Fig. 9a) provide insights into its thermal stability, decomposition behavior, and phase transformations. The TGA curve shows an initial stable region, indicating minimal weight loss at lower temperatures, suggesting that the material retains its structural integrity up to approximately 250 °C. A significant weight loss of approximately 54.2% occurs between 250 °C and 350 °C, likely due to the decomposition of organic residues, adsorbed moisture, or structural degradation of $MoSe_2$, such as selenium evaporation or oxidation (Kashyap *et al.* 2025). This weight loss corresponds to a sharp endothermic peak in the DTA curve, indicating a thermal event such as decomposition or phase transition. Above 350 °C, the TGA curve exhibits another slight weight reduction of approximately 4.3%, which may be associated with further oxidation of $MoSe_2$ to MoO_3,

driven by selenium volatilization. The corresponding DTA profile exhibited exothermic peaks, indicating possible structural rearrangement or crystallization. The gradual mass loss beyond 450 °C suggests continuous degradation or the formation of a stable oxide phase. These findings confirm that $MoSe_2$ exhibits moderate thermal stability, with significant decomposition occurring in stages owing to selenium loss and oxidation (Singh *et al.* 2021).

In the TGA curve of PPy shown in Fig. 9 (b), a relatively stable weight profile is observed across a broad temperature range, with only minimal weight loss. This suggests that PPy exhibits good thermal stability up to higher temperatures, before undergoing major decomposition. The TGA curve's stability, with only a slight weight loss of approximately 9.98%, indicates that the polymer did not undergo significant degradation or mass loss. The minimal weight loss could be attributed to the evaporation of adsorbed moisture, residual solvents, or dopants; however, the polymer backbone itself remained intact over a wide range. This behavior contrasts with that of polymers that show rapid degradation at distinct temperature steps. The absence of sharp weight-loss transitions suggests that PPy underwent gradual decomposition rather than sudden breakdown. The high thermal stability observed in the TGA curve implies that PPy retained its structure at elevated temperatures. However, despite this stability, the DTA curve indicates that thermal events occur within the material, such as phase transitions or oxidation processes, even when the mass loss remains low.

The TGA and DTA curves of MSP, shown in Fig. 9 (c), provide crucial insights into the thermal stability and decomposition behavior of the composite material. The TGA curve showed an initial stable region up to 300 °C. Beyond this point, gradual weight loss began, followed by more pronounced degradation that continued up to 500 °C. The total weight loss was approximately 28.31%. Thermal analysis showed that MSP exhibited greater thermal resistance than MS alone, indicating successful modification. PPy, by contrast, functions as a highly thermally stable matrix or additive, with minimal weight loss across the temperature range. The overall thermal behavior suggests that blending or modifying MS with materials such as PPy significantly improves thermal stability.

A quantitative comparison shows that MS undergoes a major weight loss of approximately 54.2% between 250 and 350 °C, whereas the MSP composite exhibits a total weight loss of approximately 28.31%. The comparatively lower weight loss observed for MSP indicates improved resistance to thermal degradation after PPy incorporation. Thus, the PPy-functionalized composite exhibits a modified thermal decomposition behavior with improved thermal resistance compared with pristine $MoSe_2$.

4.1.8 Electrochemical Performance Analysis

Fig. 10 depicts the cyclic voltammetry (CV) curves of the MS and MSP electrodes recorded using the I_3^-/I^- redox electrolyte.

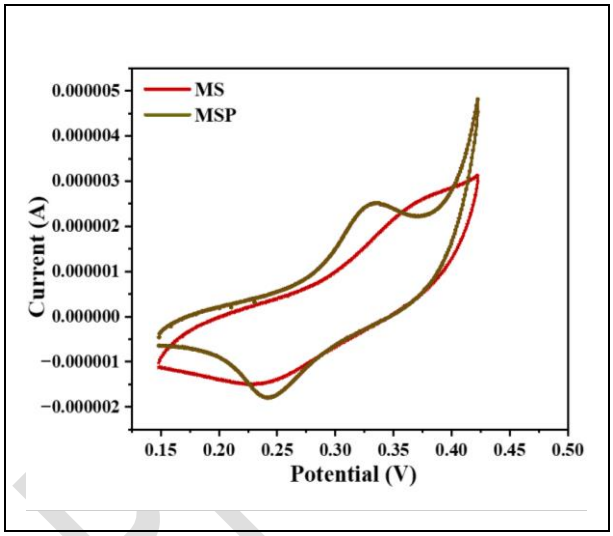

Fig. 10: CV curves of (a) MS and (b) MSP

The electrochemical measurements were performed in a three-electrode configuration, with the prepared samples as the working electrode, a Pt wire as the counter electrode, and an Ag/AgCl electrode as the reference electrode. The potential was scanned from 0.15 to 0.45 V at 40 mV s^{-1} to evaluate electrocatalytic activity toward the I_3^-/I^- redox reaction.

Both electrodes exhibit well-defined anodic and cathodic peaks corresponding to the oxidation and reduction of the I_3^-/I^- redox couple. Compared with pristine MS, the MSP electrode shows significantly higher anodic and cathodic peak currents, indicating enhanced electrocatalytic activity and faster interfacial charge-transfer kinetics. In contrast, the broader and less intense redox peaks observed for MS suggest relatively sluggish electron-transfer behavior.

The enhanced electrochemical performance of MSP is attributed to the incorporation of PPy, which increases the composite's electrical conductivity and provides an interconnected conductive network for efficient electron transport. In addition, the PPy matrix improves access to the catalytically active $MoSe_2$ sites, increasing utilization of the active surface during the redox process.

Quantitatively, the MSP electrode exhibits an anodic peak current (I_{pa}) of approximately 4.81 µA and a cathodic peak current (I_{pc}) of approximately 1.79 µA, whereas the corresponding values for MS are 3.13 µA and 1.50 µA, respectively. The anodic peak current increases by approximately 1.5 times after PPy incorporation, reflecting the enlarged electroactive

surface area and improved charge-transport pathways within the composite. Furthermore, the peak-to-peak separation (ΔE_p) decreases from approximately 195 mV for MS to 180 mV for MSP, indicating accelerated electron-transfer kinetics and improved electrochemical reversibility of the I_3^-/I^- redox couple. The increase in anodic peak current and the reduced peak-to-peak separation upon PPy incorporation are consistent with the enhanced electrocatalytic activity reported for $MoSe_2$/polymer counter-electrode composites relative to pristine $MoSe_2$ (Sowbakkiyavathi *et al.* 2020; Singh *et al.* 2021). These results demonstrate that PPy functionalization effectively enhances the electrocatalytic activity of the 2H-$MoSe_2$ electrode.

5. CONCLUSION

In summary, predominantly 2H-phase $MoSe_2$ and its PPy-functionalized composite ($MoSe_2$/PPy) were successfully synthesized *via* a rapid, energy-efficient microwave-assisted route, with PPy prepared by ultrasonic-assisted oxidative chemical polymerization. XRD confirmed hexagonal 2H-$MoSe_2$ with an average crystallite size of 50.0 nm, and retention of the characteristic $MoSe_2$ reflections together with the π–π stacking feature of PPy confirmed composite formation. FTIR and Raman spectroscopy verified the coexistence of $MoSe_2$ and PPy vibrational features, while the reduced defect-related intensity in the composite indicated favorable interfacial interaction. FE-SEM revealed a hierarchical cauliflower-like morphology in which $MoSe_2$ nanostructures were uniformly decorated with PPy, and EDX confirmed a near-ideal Mo:Se stoichiometry with successful carbon incorporation. UV–Vis analysis showed the optical band gap narrowed to 1.58 eV, compared with 1.77 eV for $MoSe_2$ and 2.01 eV for PPy, consistent with hybridization of electronic states at the polymer–chalcogenide interface. TGA demonstrated enhanced thermal stability, and CV in an I_3^-/I^- electrolyte revealed markedly higher redox peak currents for the composite than for pristine $MoSe_2$. Collectively, these results establish microwave-assisted synthesis followed by PPy functionalization as a simple and effective strategy for tailoring the properties of 2H-$MoSe_2$, highlighting $MoSe_2$/PPy as a promising counter-electrode material for dye-sensitized solar cells, supercapacitors, and sensors. Future work involving electrochemical impedance spectroscopy and long-term cycling-stability testing is required to further establish its practical potential.

DECLARATION OF COMPETING INTERESTS

The authors declare that they have no known competing financial interests or personal relationships that could have appeared to influence the work reported in this paper.

DATA AVAILABILITY

The datasets used and/or analyzed during the current study are available from the corresponding author on reasonable request.

FUNDING

This research received no specific grant from any funding agency in the public, commercial, or not-for-profit sectors.

CONFLICTS OF INTEREST

The authors declare that there is no conflict of interest.

REFERENCES

Ansari, U., Kashyap, S., Singh, A., Maken, S., Poddar, D. and Thakur, S., Investigation of Chromium and Tungsten Doped Molybdenum Di Selenide as Counter Electrode in Dye Sensitized Solar Cells for Efficient Solar Energy Conversion, *J. Power Sources,* 631, 236242 (2025). https://doi.org/10.1016/j.jpowsour.2025.236242

Balasingam, S. K., Lee, J. S. and Jun, Y., Few-Layered $MoSe_2$ Nanosheets as an Advanced Electrode Material for Supercapacitors, *Dalton Trans.,* 44(35), 15491-15498 (2015). https://doi.org/10.1039/C5DT01985K

Celik, C. G., Cogal, S., Machata, P., Uygun Oksuz, A. and Omastová, M., Electrospun Cobalt-Doped 2D-$MoSe_2$/Polypyrrole Hybrid-Based Carbon Nanofibers as Electrochemical Sensing Platforms, *Microchim. Acta,* 191(1), 1-13 (2024). https://doi.org/10.1007/s00604-023-06078-2

Chang, H., Wu, H. M., Chen, T. L., Huang, K. D., Jwo, C. S. and Lo, Y. J., Dye-Sensitized Solar Cell Using Natural Dyes Extracted from Spinach and Ipomoea, *J. Alloys Compd.,* 495(2), 606-610 (2010). https://doi.org/10.1016/j.jallcom.2009.10.057

Dai, T. J., Sun, J., Peng, X. S., Gong, J. N., Zhou, Z. Y. and Wang, X. Q., In Situ Synthesis of Heterogeneous $NiSe_2$/$MoSe_2$ Nanocomposite for High-Efficiency Electrocatalytic Hydrogen Evolution Reaction, *Energy Sci. Eng.,* 10(10), 4061-4070 (2022). https://doi.org/10.1002/ese3.1270

Dhanasekaran, G., Parthiban, N., Nithya, N., Karthigaimuthu, D., Vijayakumar, G., Sangaraju, S. and Thangavel, E., Synergistic Effects of Advanced $MoSe_2/MnO_2$ Nanocomposite: Using Direct Yellow Dye Degradation for Enhanced Photocatalytic Applications, *Inorg. Chem. Commun.,* 170, 113377 (2024). https://doi.org/10.1016/j.inoche.2024.113377

Kashyap, S., Ansari, U., Poddar, D., Singh, A., Sarkar, A. and Jain, D., Tailoring $MoSe_2$-Hybrid Polymer Composites for Optimized Electrocatalytic Activity in Dye-sensitized Solar Cells (DSSCs), *Inorg. Chem. Commun.,* 172, 113570 (2025). https://doi.org/10.1016/j.inoche.2024.113570

Ma, L., Xu, L., Zhou, X., Xu, X. and Zhang, L., Synthesis of a Hierarchical $MoSe_2$/C Hybrid with Enhanced Electrochemical Performance for Supercapacitors, *RSC Adv.,* 6(94), 91621-91628 (2016). https://doi.org/10.1039/C6RA16157J

Manimekalai, A., Thirumal, V., Kim, J., Babu, B. and Velu, K. S., Electrochemical Synthesis of Polyaniline and Sheet-like Structure of Molybdenum Selenide (PANI@2D-$MoSe_2$) Binary Composite for Solar Cell Applications, *Nanomater.,* 15(5), 384 (2025). https://doi.org/10.3390/nano15050384

Mao, B., Bao, T., Yu, J., Zheng, L., Qin, J., Yin, W. and Cao, M., One-Pot Synthesis of $MoSe_2$ Hetero-Dimensional Hybrid Self-Assembled by Nanodots and Nanosheets for Electrocatalytic Hydrogen Evolution and Photothermal Therapy, *Nano Res.,* 10(8), 2667-2682 (2017). https://doi.org/10.1007/s12274-017-1469-7

Mittal, H. and Khanuja, M., Hydrothermal In-Situ Synthesis of $MoSe_2$-Polypyrrole Nanocomposite for Efficient Photocatalytic Degradation of Dyes under Dark and Visible Light Irradiation, *Sep. Purif. Technol.,* 254, 117508 (2021). https://doi.org/10.1016/j.seppur.2020.117508

Mittal, H., Kumar, A. and Khanuja, M., In-Situ Oxidative Polymerization of Aniline on Hydrothermally Synthesized $MoSe_2$ for Enhanced Photocatalytic Degradation of Organic Dyes, *J. Saudi Chem. Soc.,* 23(7), 836-845 (2019). https://doi.org/10.1016/j.jscs.2019.02.004

Sheela, S. E., Sekar, R., Maurya, D. K., Paulraj, M. and Angaiah, S., Progress in Transition Metal Chalcogenides-Based Counter Electrode Materials for Dye-Sensitized Solar Cells, *Mater. Sci. Semicond. Process.,* 156, 107273 (2023). https://doi.org/10.1016/j.mssp.2022.107273

Siddiqui, I., Mittal, H., Kohli, V. K., Gautam, P., Ali, M. and Khanuja, M., Hydrothermally Synthesized Micron Sized, Broom-Shaped $MoSe_2$ Nanostructures for Superior Photocatalytic Water Purification, *Mater. Res. Exp.,* 5(12), 125020 (2018). https://doi.org/10.1088/2053-1591/aae241

Singh, A., Poddar, D., Thakur, S. and Jha, R., Ternary Composite Based on $MoSe_2$-RGO/Polyaniline as an Efficient Counter Electrode Catalyst for Dye-Sensitized Solar Cells, *Mater. Chem. Phys.,* 273, 125043 (2021). https://doi.org/10.1016/j.matchemphys.2021.125043

Siroha, P., Khandelwal, V., Singh, D., Ramovatar and Gangwar, J., Remarkable Enhancement in Adsorption Capacity of Methylene Blue by Hydrothermally Processed $MoSe_2$ Nanosheets for Environmental Application, *Bull. Mater. Sci.,* 47(4), 1-7 (2024). https://doi.org/10.1007/s12034-024-03307-z

Sowbakkiyavathi, E. S., Murugadoss, V., Sittaramane, R. and Angaiah, S., Development of $MoSe_2$/PANI Composite Nanofibers as an Alternative to Pt Counter Electrode to Boost the Photoconversion Efficiency of Dye Sensitized Solar Cell, *J. Solid State Electrochem.,* 24(10), 2289-2300 (2020). https://doi.org/10.1007/s10008-020-04728-6

Upadhyay, S. and Pandey, O. P., Synthesis of Layered 2H-$MoSe_2$ Nanosheets for the High-Performance Supercapacitor Electrode Material, *J. Alloys Compd.,* 857, 157522 (2021). https://doi.org/10.1016/j.jallcom.2020.157522

Vattikuti, S. V. P., Devarayapalli, K. C., Nagajyothi, P. C. and Shim, J., Microwave Synthesized Dry Leaf-like Mesoporous $MoSe_2$ Nanostructure as an Efficient Catalyst for Enhanced Hydrogen Evolution and Supercapacitor Applications, *Microchem. J.,* 153, 104446 (2020). https://doi.org/10.1016/j.microc.2019.104446

Vishnu, N. and Badhulika, S., Single Step Synthesis of $MoSe_2$-MoO_3 Heterostructure for Highly Sensitive Amperometric Detection of Nitrite in Water Samples of Industrial Areas, *Electroanal.,* 31(12), 2410-2416 (2019). https://doi.org/10.1002/elan.201900310

Wang, L., Zhao, J., Tang, X., Kuang, S., Qin, L., Lin, H. and Li, Q., Green Synthesis of $MoSe_2$ Nanosheets Based on Hydrogen Bond with High Photodegradation Performance, *Surf. Interfaces,* 39, 102956 (2023). https://doi.org/10.1016/j.surfin.2023.102956

Xu, L., Ma, L., Zhou, X., Liu, Z., Luo, D., Xu, X. and Zhang, L., Boosting Electrocatalytic Activity of Ultrathin $MoSe_2$/C Composites for Hydrogen Evolution via a Surfactant Assisted Hydrothermal Method, *Int. J. Hydrogen Energy,* 43(33), 15749-15761 (2018). https://doi.org/10.1016/j.ijhydene.2018.07.041

Zhang, K. B., Jiang, X. B., Zeng, M. and Jing, B., Hydrothermal Synthesis of Three-Dimensional Hydrangea-like $MoSe_2$@N-Doped Carbon Anode Material for High Performance Lithium Ion Batteries, *J. Electroanal. Chem.,* 879, 114818 (2020). https://doi.org/10.1016/j.jelechem.2020.114818

Zhang, X., Xue, M., Yang, X., Luo, G. and Yang, F., Hydrothermal Synthesis and Tribological Properties of $MoSe_2$ Nanoflowers, *Micro Nano Lett.,* 10(7), 339-342 (2015). https://doi.org/10.1049/mnl.2015.0014